



Power Electronic Systems
Laboratory

© 2014 IEEE

IEEE Transactions on Industrial Electronics, Vol. 61, No. 11, pp. 5974-5986, November 2014

Slotless Bearingless Disk Drive for High-Speed and High-Purity Applications

D. Steinert,
T. Nussbaumer,
J. W. Kolar

This material is published in order to provide access to research results of the Power Electronic Systems Laboratory / D-ITET / ETH Zurich. Internal or personal use of this material is permitted. However, permission to reprint/republish this material for advertising or promotional purposes or for creating new collective works for resale or redistribution must be obtained from the copyright holder. By choosing to view this document, you agree to all provisions of the copyright laws protecting it.



Eidgenössische Technische Hochschule Zürich
Swiss Federal Institute of Technology Zurich

Slotless Bearingless Disk Drive for High-Speed and High-Purity Applications

Daniel Steinert, *Student Member, IEEE*, Thomas Nussbaumer, *Member, IEEE*, and Johann W. Kolar, *Fellow, IEEE*

Abstract—In this paper, a bearingless drive for high-speed applications with high purity and special chemical demands is introduced. To achieve high rotational speeds with low losses, a slotless bearingless disk drive with toroidal windings is used. We present the working principle of the bearingless drive as well as a model for calculating the achievable drive torque. An advantageous winding system for independent force and torque generation is proposed, which can be realized with standard inverter technology. Additionally, the winding inductances are examined to evaluate the dynamic properties of bearing and drive. The findings are verified with simulation results and the system performance is successfully demonstrated on an experimental prototype, which runs up to 20 000 rpm and is designed for an output power of 1 kW.

Index Terms—Active magnetic bearing, bearingless motor, high-speed drive, slotless motor.

I. INTRODUCTION

In a bearingless motor the rotor is levitated magnetically without mechanical contact, whereas the functionality of bearing force and drive torque generation is combined in the motor [1], [2]. This technology appears in more and more applications, where high purity and hygiene [3], high rotational speeds [4], chemical resistance [5], [6], or absence of friction and low maintenance [7] is demanded. Possible applications of the proposed motor topology might be pumps, compressors, or ventilators for chemical aggressive or highly pure mediums. Additionally, the motor can be used as drive for a rotor, which rotates in a hermetically sealed chamber [8].

Problems arise for conventional motors, when the device is used in highly aggressive environments, as seals and bearings are destroyed and the lifetime of the motor is shortened. The bearingless motor concept offers the possibility of omitting mechanical bearings and encapsulating the levitated rotor inside a gas-tight environment. Thus, chemical resistance can be achieved. Additionally, it also satisfies ultra-high purity demands, as they exist for example in the semiconductor, pharmaceutical, and biomedical industry.

Manuscript received June 4, 2013; revised September 16, 2013, December 2, 2013, and January 29, 2014; accepted February 7, 2014. Date of publication March 12, 2014; date of current version June 6, 2014.

D. Steinert and J. W. Kolar are with the Power Electronic Systems Laboratory, Swiss Federal Institute of Technology (ETH) Zurich, CH-8092 Zurich, Switzerland (e-mail: steinert@lem.ee.ethz.ch; kolar@lem.ee.ethz.ch).

T. Nussbaumer is with Levitronix GmbH, CH-8005 Zurich, Switzerland (e-mail: nussbaumer@levitronix.com).

Color versions of one or more of the figures in this paper are available online at <http://ieeexplore.ieee.org>.

Digital Object Identifier 10.1109/TIE.2014.2311379

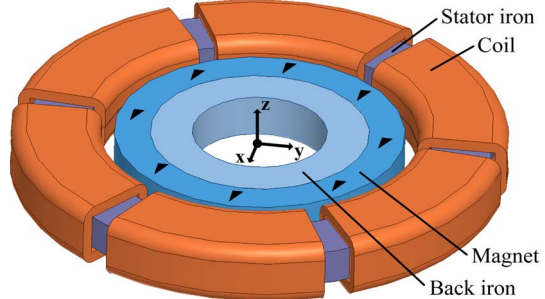


Fig. 1. Principle setup of slotless disk motor. The rotor consists of a diametrically magnetized ring magnet (the magnetization is indicated by the arrows) and a back iron. The annular rotor has six toroidally wound coils for force and torque generation.

The bearingless disk motor topology (see Fig. 1) combines bearing and brushless motor in one stator [9]. No driveshaft and no mechanical bearings are needed. Therefore, a simple and compact design can be realized, that can be easily sealed and has low maintenance effort. Moreover, this topology can be implemented as hollow shaft rotor, where air or fluid can pass the rotor. Conventional bearingless motor designs typically have slotted stators, as for example bearingless switched reluctance motors [10], or slotted permanent magnet bearingless motors [11]. These topologies show good performance in regard to achievable force and torque, as the magnetic flux is guided by the slots. With higher rotational speeds and surface speeds, these slots cause higher eddy current and hysteresis losses because of field harmonics in the rotor and in the stator. In particular, the eddy current losses in the retaining sleeve of the rotor and in the rotor magnet may get massive at high rotational speeds, as is shown in [12]. As permanent magnets with high energy density are necessary to achieve a good passive bearing stability, the problem increases even more.

In the literature, as for example in [13] and [14], slotless topologies are proposed, that promise low losses due to the lack of field fluctuations in the rotor as well as a compact design. In these machines, radial-flux-linkage air-core coils are used, which require the connection of each two wires leading back and forth in the air gap. For common rotors with small diameters compared to its length, this leads to a good utilization of the copper, as only the connection of back and forth wire lies outside the rotor. For toroidal windings, where the return wire lies outside the stator, the unused wire length is defined by the stator height and thickness. In the case of a disk drive with large diameters, toroidal windings will result in a better utilization of the copper and thus in lower copper losses. A comparison of an exemplary air gap winding with a toroidal winding is shown in

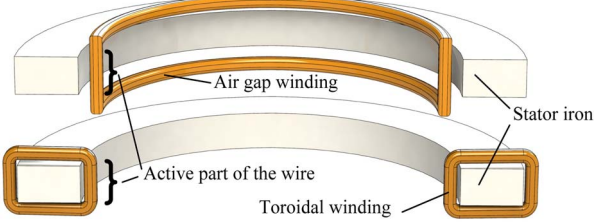


Fig. 2. Schematic drawing of one exemplarily radial-flux-linkage air gap winding (top) and one toroidal winding (bottom) for generation of a two pole magnetic field. It can be seen that the unused copper length is smaller in the toroidal winding because of the large diameter of the stator.

Fig. 2. As toroidal wires do not require that each two coil sides in the air gap are connected, it allows for independent control of each coil. For that reason, the specific winding configuration proposed in this paper would not be feasible with radial-flux-linkage coils, as no independent force and torque control would be possible.

A disk drive with toroidal windings has already been proposed with a five-phase winding system with ten stator coils [15]–[17]. Here, each two coils are connected in series. The minimal number of one pole pair in the rotor leads to low electric frequencies even for high rotational speeds.

Reducing the coil number to six enhances the simplicity of the topology and improves the possibility to arrange position sensors in the air gap, as there is more space in between the coils. As each three coils can be connected in a star point, standard inverter technology with two three-phase inverters can be used. Moreover, simulations show that the six coil topology, as presented in this paper, generates about 20% more torque with the same current and therefore promises a higher performance.

Bearingless motors with toroidal windings were first proposed in [18] and [19] to be used in motors with low axial length. As these machines have consequent poles, they are particularly suitable for low-speed applications. In [20], a slotless machine is proposed where discontinuous coil currents are used for bearing and drive control, which is not feasible for higher speeds, either.

In this paper, a slotless bearingless disk drive is shown with a new type of toroidal winding concept, where six coils are controlled with two three-phase current systems. This leads to a low hardware effort, high control simplicity, good manufacturability, and high performance. Each three coils can be connected to a star point, so that two standard three-phase inverters can be used. That means 12 power switches in total and only four current sensors. Moreover, the big rotor diameter of the presented prototype allows for a high power output that is needed for example in blower applications.

In Sections II and III, the basic concept of the bearingless motor will be introduced and the working principle of bearing force and drive torque generation will be examined in detail. In Section IV, inductance of the coils regarding bearing and drive currents are examined, to assess the dynamic properties of the topology. Based on FE simulations, the bearing and motor properties of the topology are presented in Section V. Finally, the performance of the system will be verified on an experimental prototype until 20 000 r/min in Section VI.

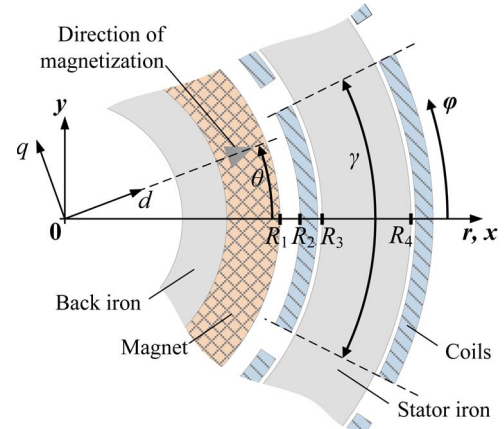


Fig. 3. Definition of the Cartesian and polar coordinate systems fixed to the stator (x, y, φ, r) and the axes d and q of the coordinate system fixed to the rotor. The rotor angle θ is the angle between the x -axis and the axis of magnetization d . $R_{1..4}$ are the radii of rotor, coils, and stator; γ is the opening angle of the coils.

II. BASIC SETUP OF THE SLOTLESS DISK MOTOR

The proposed topology combines motor and magnetic bearing at one shared magnetic circuit. In contrast to the most bearingless motor applications with slotted stator, the coils are wound in circumferential direction around a ring-shaped stator (see Fig. 1). To reduce the occurring frequencies, the rotor has only one magnetic pole pair with diametrical magnetization. Therefore, a sinusoidal magnetic field penetrates the coils, where forces can be generated due to the Lorentz effect.

As the stator has no magnets and no slots, the magnetic field actively generated in the air gap by the stator is very homogeneous and small compared to a slotted stator, where the flux is concentrated at the teeth. Additionally, the rotor rotates with the same speed as the magnetic field for the drive. Consequently, the rotor will see very little magnetic field fluctuation, whereas very low losses shall occur in the rotor. However, losses from time harmonic field fluctuations caused by the inverter carrier frequency might be apparent in the rotor as well as air friction losses. The stator is penetrated by the rotating field of the rotor, which requires a laminated stator core in order to minimize eddy current losses in the stator.

For the description of displacements and forces we introduce a Cartesian coordinate system (x, y) and a polar coordinate system (r, φ) which are both fixed to the stator (see Fig. 3). The axis d defines the axis of magnetization and is fixed to the rotor. The angle θ gives the angular position of the rotor and is defined as the angle between x - and d -axes.

The stability of the rotor against axial deflection and tilting is given by passive reluctance forces according to the disk type principle [21]. A deflection in axial direction causes a counteracting force, as well as a tilting of the rotor results in a torque against the tilting direction (see Fig. 4). As the height of the rotor is significantly smaller than its diameter, the gyroscopic effect stabilizes the rotor additionally against tilting at higher rotational speeds [16].

The passive bearing capabilities of the topology can be described with the axial stiffness

$$c_z = \frac{dF_z}{dz} \quad (1)$$

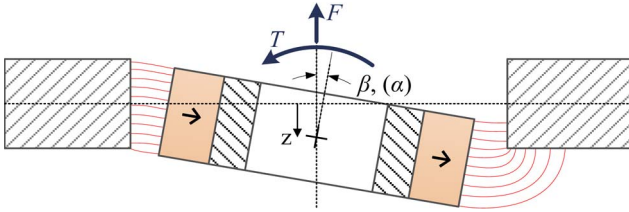


Fig. 4. Stabilizing passive bearing force and torque resulting from axial deflection z and tilting β around axis perpendicular to magnetization.

and the tilting stiffness

$$c_\alpha = \frac{dT_\alpha}{d\alpha} \text{ and } c_\beta = \frac{dT_\beta}{d\beta} \quad (2)$$

where α and β are the tilting angles around and perpendicular to the magnetization axis, respectively. As there are only two magnetic poles, rotation around the direction of magnetization results in a smaller stiffness than rotation perpendicular to the magnetization.

In some applications, as for example in pumps and blowers, the bearing has to compensate high axial forces and tilting torques, which occur during operation, and therefore is one aim for the optimization of such a bearingless motor to improve this passive stiffness values. Higher stiffnesses will result in lower deflections at the same disturbing forces, which enhance the performance under load conditions.

In contrast to the tilting and the axial shift, a radial displacement results in a destabilizing force that pulls the rotor further away from the center position. Again, the two magnetic poles result in anisotropic radial stiffness, whereas the stiffness in the direction of magnetization

$$c_d = \left. \frac{dF_x}{dx} \right|_{\theta=0} \quad (3)$$

is bigger than the stiffness perpendicular to the magnetization

$$c_q = \left. \frac{dF_y}{dy} \right|_{\theta=0}. \quad (4)$$

To stabilize the bearing, an active generation of radial bearing forces is required, counteracting the passive attractive forces.

III. FORCE AND TORQUE GENERATION

A. Analytic Lorentz Force Calculation

To find appropriate current commands for controlling drive torque and bearing forces independently, the Lorentz forces in the coils are considered. The magnetic flux in the air gap penetrates the coils, whereas a force in each coil perpendicular to the coil current density J and the B-field results according to the Lorentz force law

$$\vec{F} = \int (\vec{J} \times \vec{B}) dV. \quad (5)$$

As the permanent magnet ring is magnetized diametrically, the magnetic air gap field has a sinusoidal distribution in circumferential direction. Because of the small air gap in

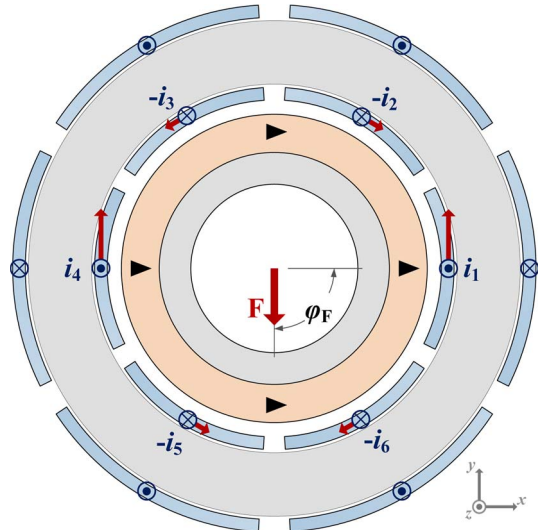


Fig. 5. Principle of suspension force generation at rotor position $\theta = 0^\circ$ and force direction $\varphi_F = 90^\circ$. The currents (indicated by circles) of opposite coils are flowing in the same direction, generating forces, which are also pointing in the same direction (indicated by arrows). This leads to a total reacting force F on the rotor without any torque. Here, the sum of all currents is zero to enable a star connection of the six coils. Positive currents are defined as flowing in positive z -direction at the inner side of the stator.

comparison to the diameter of the magnet, the tangential component of the B-field can be neglected with regard to the radial component. Therefore, only the radial flux density component is considered, which can be written as

$$B_{\text{rad}} = \hat{B}_{\text{rad}} \cos(\varphi - \theta) \quad (6)$$

with the peak value \hat{B}_{rad} . The angle θ defines the angular rotor position; φ is the angular coordinate in the polar coordinate system. For a solid magnet disk inside an annular stator iron, the flux field can be calculated analytically, as it is shown in [22]. As the field calculation for a magnet ring with backiron is much more sophisticated, \hat{B}_{rad} is determined by magnetic simulations.

In order to be able to control the bearing force and drive torque independently, appropriate coil current commands for the given assembly have to be found. Considering the Lorentz forces in opposite stator coils, it can be shown with (5) and (6) that a force acts on the rotor, if the currents in opposite coils point in the same direction. If opposite coils are energized in opposite direction, a drive torque will result without a force

$$\begin{aligned} J(\varphi) = J(\varphi + 180^\circ) &\Rightarrow T = 0, \quad \vec{F} = \text{variable} \\ J(\varphi) = -J(\varphi + 180^\circ) &\Rightarrow \vec{F} = 0, \quad T = \text{variable}. \end{aligned} \quad (7)$$

This means that torque and force can be controlled independently at any rotor position. In Figs. 5 and 6, the principles of force and torque generation are shown. It can be seen that with the same set of coils, force and torque can be generated. Now it is necessary to develop the right current commands for independent control of force and torque.

Having in total six coils available, six bearing currents plus six drive currents can be superposed. Both bearing and drive

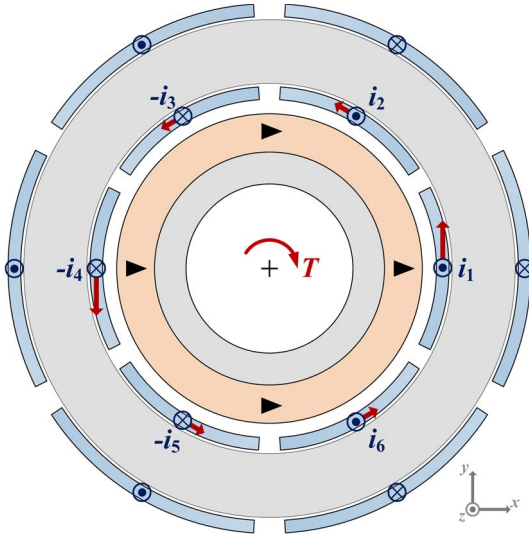


Fig. 6. Principle of drive torque generation at rotor position $\theta = 0^\circ$. Here, the currents of opposite coils flow in the opposite direction. With the forces pointing also in opposite directions, a reacting torque T acts on the rotor without any force. The sum of all currents is again zero. Positive currents are defined as flowing in positive z -direction at the inner side of the stator.

system can be realized advantageously by a symmetrical three-phase system

$$\begin{aligned} i_{B,1} &= \hat{I}_B \cdot \sin(\theta + \varphi_B) \\ i_{B,2} &= \hat{I}_B \cdot \sin\left(\theta - \frac{2}{3}\pi + \varphi_B\right) \\ i_{B,3} &= \hat{I}_B \cdot \sin\left(\theta + \frac{2}{3}\pi + \varphi_B\right) \end{aligned} \quad (8)$$

$$\begin{aligned} i_{D,1} &= \hat{I}_D \cdot \cos(\theta) \\ i_{D,2} &= \hat{I}_D \cdot \cos\left(\theta - \frac{2}{3}\pi\right) \\ i_{D,3} &= \hat{I}_D \cdot \cos\left(\theta + \frac{2}{3}\pi\right) \end{aligned} \quad (9)$$

whereby the individual currents are superposed on the coils as follows:

$$\begin{aligned} i_1 &= i_{B,1} + i_{D,1} & i_4 &= i_{B,1} - i_{D,1} \\ i_2 &= i_{B,2} - i_{D,3} & i_5 &= i_{B,2} + i_{D,3} \\ i_3 &= i_{B,3} + i_{D,2} & i_6 &= i_{B,3} - i_{D,2}. \end{aligned} \quad (10)$$

As will be shown further, the two current systems $i_{B,n}$ (8) for the force generation and $i_{D,n}$ (9) for the torque generation result in constant force with direction φ_F and constant torque. The superposition of the currents according to (10) fulfills the conditions in (7). Furthermore, these six coil currents form again two separate symmetrical three-phase systems

$$\begin{aligned} i_1 + i_3 + i_5 &= 0 \\ i_2 + i_4 + i_6 &= 0, \end{aligned} \quad (11)$$

which can be controlled by two independent three-phase inverters. In Fig. 7, the connection scheme of the coils to the power electronics is shown. In total, 12 power switches and four current sensors are necessary, as only two currents in each system are independent.

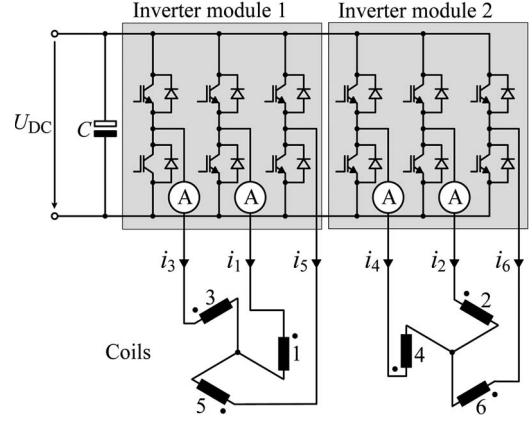


Fig. 7. Schematic circuit of the power electronics consisting of two inverter modules with six power switches each. Each module powers three coils, connected to a star point. Therefore, only two current sensors per module are necessary. The modules are fed by the dc link voltage U_{DC} . For a better comprehension, the coils are drawn according to their position on the stator.

With (5), the resulting total force acting on the stator coils

$$\vec{F} = h \iint_{ACu} (\vec{J} \times \vec{B}_{rad}) dA \quad (12)$$

can be obtained by integrating over the cross-section area ACu of the coils within the stator core. Here, it is assumed, that B_{rad} is constant over the height h of the rotor. This means, that any stray flux in axial direction is neglected. In the same way, the total drive torque

$$\vec{T} = h \iint_{ACu} \vec{r} \times (\vec{J} \times \vec{B}_{rad}) dA \quad (13)$$

can be calculated by including the radius r of the occurring Lorentz forces.

For simplification it will be assumed, that the coils are infinitely thin with a mean radius

$$R_m = \frac{R_2 + R_3}{2}. \quad (14)$$

By converting the current commands (8) and (9) into a line current density and subsequent integration of the Lorentz forces according to (12) and (13), force and torque result in

$$\vec{F}_{bng,L} = k_{F,L} \cdot \hat{I}_B \left(\begin{array}{c} \cos(\varphi_F) \vec{e}_x \\ \sin(\varphi_F) \vec{e}_y \end{array} \right) \quad (15)$$

$$T = k_T \cdot \hat{I}_D \quad (16)$$

with the Lorentz force coefficient

$$k_{F,L} = \frac{3}{2} \hat{B}_{rad} \cdot N \cdot h \cdot \frac{\sin \gamma}{\gamma} \quad (17)$$

and the torque coefficient

$$k_T = 6 \hat{B}_{rad} \cdot N \cdot h \cdot R_m \cdot \frac{1}{\gamma} \sin\left(\frac{\gamma}{2}\right). \quad (18)$$

Here, \vec{e}_x and \vec{e}_y are the unit vectors in x - and y -direction, γ is the angle width of the coil and N the number of turns per coil.

TABLE I
COMPARISON OF ANALYTICAL LORENTZ FORCES
AND 2-D SIMULATION RESULTS

Parameter	2D Simulation	Lorentz force calculation
flux density	B_{rad}	673 mT
Forces for bearing current $\hat{I}_B = 100 \text{ A}\cdot\text{turns}$		
... on stator iron	$F_{\text{bng,R}}$	1.51 N
... on coils	$F_{\text{bng,L}}$	1.32 N
... on rotor	F_{bng}	-2.82 N
Torque for drive current $\hat{I}_D = 100 \text{ A}\cdot\text{turns}$		
... on rotor	T	-0.156 Nm
		-0.160 Nm

B. Reluctance Forces

In addition to the Lorentz Forces calculated above, reluctance forces acting on the stator iron have to be considered for the bearing forces. By energizing the coils with a bearing current, a magnetic field with four poles is generated that is superposed to the magnetic two-pole field of the permanent magnet. Therefore, the flux density in the air gap is weakened at one side of the rotor and strengthened on the other. This results in a force on the stator iron in radial direction. To assess this effect, two-dimensional (2-D) finite element simulations have been conducted. The results show, that the reluctance force $F_{\text{bng,R}}$ acts in the same direction as the Lorentz force $F_{\text{bng,L}}$ for this setup. The total bearing force then results in

$$F_{\text{bng}} = F_{\text{bng,L}} + F_{\text{bng,R}}. \quad (19)$$

The linear dependency of bearing force and bearing current

$$\vec{F}_{\text{bng}} = k_F \cdot \hat{I}_B \begin{pmatrix} \cos(\varphi_F) \vec{e}_x \\ \sin(\varphi_F) \vec{e}_y \end{pmatrix} \quad (20)$$

with the bearing force coefficient k_F is still given with the reluctance forces included, as will be shown in Section V by three-dimensional (3-D) simulations.

Table I shows a comparison of the calculated Lorentz forces and the simulated forces acting on stator iron, coils, and rotor. Basis for the analytical Lorentz force calculation is the B-field achieved by 2-D simulation. This calculated force fits very well to the simulated force acting on the coils. However, the reluctance force acting on the iron is in a similar range as the Lorentz forces for the given dimensions. The resulting bearing force acting on the rotor is the sum of Lorentz forces in the coils and reluctance forces in the stator iron (see Table I).

As the reluctance forces only act in radial direction, they will not generate any torque. Therefore, analytical and simulated torque acting on the rotor coincide.

Summarizing, the theoretical considerations are confirmed by the simulation results. By superposition of two three-phase current systems, bearing force and drive torque are directly proportional to the amplitudes \hat{I}_B and \hat{I}_D , whereas the phase shift φ_F defines the force direction. The bearing force not only results from Lorentz forces, but also from reluctance effects. Force and torque are constant over the angular rotor position.

Additionally, it has to be considered that 2-D analysis and simulation neglect any flux in axial direction. Therefore, in flat

motors, the magnetic field as well as force and torque will be higher in the 2-D analysis than in the 3-D structure, as will be seen in Section V. However, this does not affect the functionality of the motor.

IV. INDUCTANCES OF BEARING AND DRIVE SYSTEM

The knowledge of the inductances of the system is important to determine the necessary inverter voltage and to evaluate the dynamics of bearing and motor. Additionally, it can be used to design the current controller of the inverter.

A. Analytical Calculation

As in the toroidal winding structure, there are conductors outside of the stator core, and the self-inductance of one coil is comparably high. However, not only the self-inductances but also the mutual inductances act together with all coil currents. Therefore, their influence on the voltage has to be considered.

We assume that no saturation occurs in the stator. The flux linkage Ψ_k in each coil k consists of a flux part from the permanent magnet $\Psi_{k,\text{PM}}$ and a flux linkage in coil k due to the currents of all coils $\Psi_{k,\text{I}}$

$$\Psi_k = \Psi_{k,\text{PM}} + \Psi_{k,\text{I}}. \quad (21)$$

Hereby, $\Psi_{k,\text{I}}$ is given by

$$\Psi_{k,\text{I}} = \sum_n L_{kn} \cdot i_n \quad (22)$$

whereas L_{kn} is the inductance matrix, and i_n the coil currents. Here, n is the number of the active coil and k the coil, where the related voltage is induced. The armature flux linkage $\Psi_{k,\text{I}}$ is the combined flux in coil k generated by all coil currents. All inductances are positive, as the winding direction and positive current direction are the same in all coils.

For coil 1, this results in

$$\Psi_{1,\text{I}} = L_{11}i_1 + L_{12}i_2 + L_{13}i_3 + L_{14}i_4 + L_{15}i_5 + L_{16}i_6 \quad (23)$$

and by inserting the current commands (10) we obtain

$$\Psi_{1,\text{I}} = \Psi_{1,\text{B}} + \Psi_{1,\text{D}} \quad (24)$$

with the flux linkage $\Psi_{1,\text{B}}$ resulting from the bearing currents

$$\begin{aligned} \Psi_{1,\text{B}} &= (L_{11} + L_{14})i_{\text{B},1} + (L_{12} + L_{15})i_{\text{B},2} \\ &\quad + (L_{13} + L_{16})i_{\text{B},3} \end{aligned} \quad (25)$$

$$\begin{aligned} \Psi_{1,\text{D}} &= (L_{11} - L_{14})i_{\text{D},1} + (L_{13} - L_{16})i_{\text{D},2} \\ &\quad + (L_{15} - L_{12})i_{\text{D},3} \end{aligned} \quad (26)$$

the flux linkage from the drive currents. Here, it gets clear that the flux linkages resulting from bearing and motor currents can be superposed independently.

Assuming that the self-inductances of each coil and the mutual inductances of coils with the same distance are equal, we can simplify

$$L_0 = L_{11} = L_{22} = \dots \quad (\text{self-inductance})$$

$$L_1 = L_{12} = L_{23} = \dots \quad (\text{mutual inductance of adjacent coils})$$

$$L_2 = L_{13} = L_{24} = \dots \quad (\text{mutual ind. of coils with distance 2})$$

$$L_3 = L_{14} = L_{25} = L_{36} \quad (\text{mutual inductance of opposite coils}).$$

Again, we want to point out that this model is analytically correct in the case that the iron core is not saturated and, therefore, the material behavior is linear.

Then, the induced flux linkage components are

$$\Psi_{1,B} = (L_0 + L_3)i_{B,1} + (L_1 + L_2)(i_{B,2} + i_{B,3}) \quad (27)$$

$$\Psi_{1,D} = (L_0 - L_3)i_{D,1} + (L_2 - L_1)(i_{D,2} + i_{D,3}) \quad (28)$$

and as the sum of the bearing currents as well as the sum of the motor currents is zero, we can substitute

$$\begin{aligned} i_{B,2} + i_{B,3} &= -i_{B,1} \\ i_{D,2} + i_{D,3} &= -i_{D,1}. \end{aligned} \quad (29)$$

This simplifies the armature flux linkage components to

$$\Psi_{1,B} = (L_0 - L_1 - L_2 + L_3)i_{B,1} = L_B i_{B,1} \quad (30)$$

$$\Psi_{1,D} = (L_0 + L_1 - L_2 - L_3)i_{D,1} = L_D i_{D,1} \quad (31)$$

and we can introduce L_B being the inductance for bearing currents and L_D the inductance for drive currents. With this, it is also proven that the flux induced in one coil only depends on the bearing and drive current in this respective coil, assuming that all other coils are energized according to the specified current commands.

This can be also seen when looking at the voltage across the coil. By differentiating the flux linkage (21) and (24) with respect to the time, we obtain

$$u_1 = \frac{d\Psi_1}{dt} = \frac{d\Psi_1}{di_{B,1}} \frac{di_{B,1}}{dt} + \frac{d\Psi_1}{di_{D,1}} \frac{di_{D,1}}{dt} + \frac{d\Psi_{1,PM}}{dt} \quad (32)$$

which is the voltage in coil 1 resulting from bearing and motor current as well as from the permanent magnet. Inserting (30) and (31), we obtain

$$u_1 = L_B \frac{di_{B,1}}{dt} + L_D \frac{di_{D,1}}{dt} + \frac{d\Psi_{1,PM}}{dt} \quad (33)$$

and it can be seen, that bearing and drive current independently induce a voltage according to their inductance value. As all six coils on the motor are identical, the results can be adopted for every coil. Therefore, the current in one coil

$$u = u_{L,B}(i_B) + u_{L,D}(i_D) + u_{\text{ind}}(\theta, x, y) \quad (34)$$

consists of a bearing and drive inductance voltage $u_{L,B}$ and $u_{L,D}$ depending on the bearing or drive current. Additionally, an induced EMF voltage u_{ind} results from the rotation and the radial movement of the permanent magnet rotor. The voltage resulting from the resistance of the coils is neglected here.

It is important to see that bearing and drive inductances

$$L_B = L_0 - L_1 - L_2 + L_3 = u_{L,B} \cdot \left(\frac{di_B}{dt} \right)^{-1} \quad (35)$$

$$L_D = L_0 + L_1 - L_2 - L_3 = u_{L,D} \cdot \left(\frac{di_D}{dt} \right)^{-1} \quad (36)$$

are generally different. This can be explained, as with the bearing currents a four-pole magnetic field is generated, whereas the drive currents generate a two-pole magnetic field. Another interesting aspect is, that the bearing and drive inductances can also be smaller than the self-inductance. This is particularly the case if the mutual inductances are in the range of the self-inductance, which can be seen further down.

B. Evaluating the Bearing Dynamics

The stability of the system not only depends on the stiffnesses, but also on the dynamics of the bearing forces, which is limited by the inductance of the coils. To counteract an arbitrary external disturbing force, a bearing force has to be applied on the rotor much quicker than the inertial mass of the rotor reacts. The maximal achievable slew rate of the bearing current is determined by the bearing inductance and the maximal available voltage. With this, the electrical time constant of the bearing

$$\tau_{\text{el},B} = \frac{\hat{I}_B}{U_B} \cdot L_B, \quad U_B = \frac{U_{\text{DC}}}{\sqrt{3}} - \hat{U}_{\text{ind}}(n_{\max}) \quad (37)$$

can be defined, which is the time needed to apply the bearing current \hat{I}_B with the available voltage for the bearing U_B . This voltage depends on the dc link voltage U_{DC} and the peak value of the induced EMF voltage \hat{U}_{ind} at maximum speed n_{\max} . To obtain bearing stability, this time has to be smaller than the mechanical time constant

$$\tau_{\text{mech},B} = \sqrt{\frac{m}{|c_{\text{rad}}|}} \quad (38)$$

$$\tau_{\text{el},B} < \tau_{\text{mech},B}. \quad (39)$$

Here, m is the mass of the rotor and c_{rad} the radial stiffness. This means that a bearing force current I_B must be established faster by the maximal available voltage U_B over the inductance than the effect of a disturbing force takes place. Therefore, the bearing inductance L_B should be as small as possible.

Doing a worst case approximation for the prototype shown in Section VI, we suppose a maximal bearing current of $\hat{I}_B = 7.4 \text{ A}$ corresponding to the simulated startup current, while the rotor spins with maximal rotational speed. The induced voltage

$$\hat{U}_{\text{ind}} = \frac{2}{3}\pi n k_T = 97.7 \text{ V} \quad (40)$$

can be calculated by the torque coefficient k_T at the maximum rotational speed n of 20 000 rpm. With a dc link voltage of 325 V, the electrical time constant results with (37) in

$$\tau_{\text{el},B} = 0.08 \text{ ms}.$$

TABLE II
MEASURED INDUCTANCES OF THE PROTOTYPE WITHOUT ROTOR
AND CALCULATED VALUES FOR DRIVE AND BEARING

Inductance	measured	calculated*
self-inductance	L_0	3.59 mH
mutual ind. of adjacent coils	L_1	2.39 mH
mutual ind. of coils with dist. 2	L_2	1.73 mH
mutual ind. of opposite coils	L_3	1.52 mH
bearing inductance	L_B	1.05 mH
drive inductance	L_D	2.62 mH
		2.73 mH

* Calculated from measured $L_0..L_3$ according to (35),(36)

The mechanical time constant for the prototype results in

$$\tau_{\text{mech},B} = 6.8 \text{ ms}$$

taking into account the mass and radial stiffness shown in Tables IV and V.

Therefore, the electrical time constant is smaller than the mechanical time constant by a factor greater than ten. As during normal operation, the occurring bearing currents are far smaller than the startup current, and the electrical time constant is even lower.

C. Measurements

To prove the calculations and to assess the bearing capability, measurements have been conducted with the prototype, which is described in Section VI.

Measuring the inductance values for bearing and drive is related with some measurement effort. It requires applying a three-phase sine voltage either in bearing or in drive configuration, respectively. For this experiment, each two opposite coils are connected in series to ensure that only bearing current I_B or drive current I_D is flowing, depending on the direction of the series connection. This is only possible while the rotor is removed or locked in the center position. A three-phase voltage is then applied to the resulting three phases.

The regarding inductances

$$L_B = \frac{U}{I_B} \cdot \frac{\sin(\varphi)}{2\pi f} \quad (\text{at } I_D = 0) \quad (41)$$

$$L_D = \frac{U}{I_D} \cdot \frac{\sin(\varphi)}{2\pi f} \quad (\text{at } I_B = 0) \quad (42)$$

can be calculated by measuring the voltage U at one coil, the resulting current I_B or I_D , the phase shift φ between voltage and current at the coil, and the frequency f of the applied voltage.

With the proposed (35) and (36), a simple alternative method is available for easily calculating bearing and drive inductance out of the self- and mutual inductances, which can be easily measured with an LCR-meter and by measuring the voltage transfer ratio between the coils.

The results are shown in Tables II and III. Both the self- and mutual inductances as well as the bearing and motor inductance have been measured. It shows that the measured bearing and drive inductance fit very well with the values calculated from the self- and mutual inductances. Therefore, the theoretical formulas are proven.

TABLE III
MEASURED AND CALCULATED INDUCTANCES OF THE PROTOTYPE WITH ROTOR (AVERAGE OVER ROTOR ANGLE) FOR DRIVE AND BEARING

Inductance	measured	calculated*
self-inductance	L_0	2.05 mH
mutual ind. of adjacent coils	L_1	0.92 mH
mutual ind. of coils with dist. 2	L_2	0.56 mH
mutual ind. of opposite coils	L_3	0.45 mH
bearing inductance	L_B	0.92 mH
drive inductance	L_D	2.01 mH

* Calculated from measured $L_0..L_3$ according to (35),(36)

It also can be seen that both bearing and drive inductance are smaller than the self-inductance of a single coil. In particular, the low-bearing inductance enables a fast control of the bearing forces.

The measurements have been conducted with and without the rotor inserted in the stator. The magnetic flux from the rotor partially saturates the stator and influences the inductance values, which are then dependent on the rotor angle. For the measurement with rotor, the values are averaged over the rotor angle. It shows that with the rotor the self- and mutual inductances are lowered significantly for remote coils even to about one third of the value. This is due to the partial saturation of the stator iron due to the strong permanent magnets on the rotor. However, the bearing and drive inductances are not so much lowered and approximately fit to the values measured without rotor. Interestingly, the calculated values from the self- and mutual inductances fit very well with the measured values also in case of the partial stator saturation.

Therefore, it can be concluded, that by measuring the self- and mutual inductances of the coils, the bearing and drive inductance can be derived easily without complex three-phase measurements. These values are useful for assessing the dynamics of the bearing as well as for designing the controller algorithms.

This approach can be easily applied to other slotless topologies with different coil and pole pair numbers.

V. SIMULATION AND GEOMETRY PARAMETERS

To examine different geometry parameters for the prototype and to validate the theoretical considerations, 3-D finite element simulations have been conducted with an electromagnetic field simulation software. The geometry parameters of the simulated design are shown in Table IV. They result from optimizations to achieve higher axial and tilting stiffness values taking into account the manufacturability. This is also the same design as used for the prototype (see Section VI).

In Fig. 8, the magnetic field distribution in a cross section through the air gap is shown. It can be seen that the flux density varies over the height of the air gap and that due to the low length of the motor, the axial stray flux is considerably high. Table V shows the 3-D simulation results for the bearing and drive properties of the prototype compared to the 2-D results. It shows that the radial flux density in the air gap \hat{B}_{rad} is higher in 2-D due to the neglected axial stray flux. This results in force and torque values that are about 20% higher in 2-D than in the

TABLE IV
GEOMETRY PARAMETERS OF THE PROTOTYPE

Parameter	Value
outer rotor diameter (including retaining sleeve)	102 mm
rotor magnet height	15 mm
stator iron height	12.5 mm
rotor weight	880 g
outer diameter of stator iron	156 mm
magnetic gap (between magnet and stator iron)	9.5 mm
rotor encapsulation	2.5 mm
stator encapsulation	1 mm
Coil thickness (including insulation)	5 mm
free air gap	1 mm
Number of turns per coil	112
Wire diameter	1 mm
Current density at 1 A	1.27 A/mm ²
rated speed	20 000 r/min

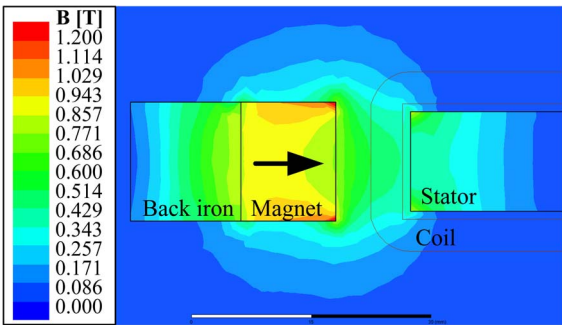


Fig. 8. Numeric 3-D simulation of the magnetic field distribution in a cross section through back iron, magnet, coil, and stator. All currents are zero.

TABLE V
2-D AND 3-D SIMULATION RESULTS OF THE BEARINGLESS MOTOR

Parameter	2D	3D
max. air gap flux density	\hat{B}_{rad}	673 mT
force coefficient	k_F	3.16 N/A
torque coefficient	k_T	0.175 Nm/A
startup current	$\hat{I}_{B,\text{start}}$	7.4 A
radial stiffness	c_d	-19 N/mm
	c_q	-10 N/mm
tilting stiffness	c_α	0.11 Nm/deg
	c_β	0.30 Nm/deg
axial stiffness	c_z	8.6 N/mm

** the flux density varies over the height of the air gap

3-D simulation. As will be shown in Section VI, the measured values fit quite well with the 3-D simulation results.

In Figs. 9 and 10, the simulated bearing force and drive torque during a half turn of the rotor are shown for a constant drive and bearing current, respectively. As expected, with the given current commands as detailed in Section III, the simulation shows constant torque and nearly constant force characteristics independently of the rotor angle. The small ripple in the bearing force results from the partial saturation of the stator iron. Additionally, no force is generated by a drive current and vice versa. In Fig. 11, it is shown that bearing force and drive torque depend linearly on the respective current. Saturation effects are negligible and occur only far beyond the used currents.

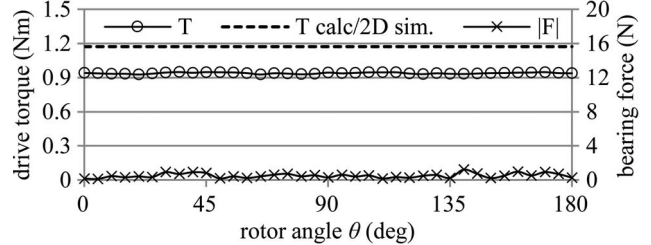


Fig. 9. Simulated torque and absolute force on the rotor over a half turn of the rotor with a drive current of $\hat{I}_D = 6.7$ A. The simulated force on the rotor is very small and is supposed to be only simulation noise, as it is random and has no periodicity. The dashed line shows the torque obtained by 2-D simulation and calculation.

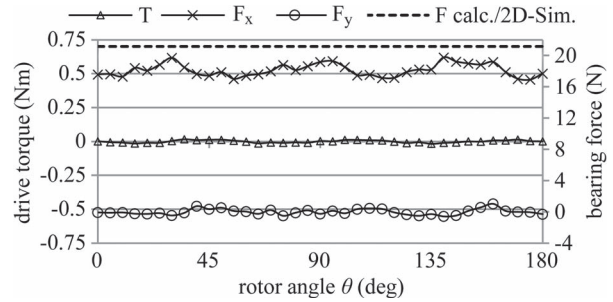


Fig. 10. Simulated torque and bearing force in x and y -direction over a half turn of the rotor with a bearing current of $\hat{I}_B = 6.7$ A and force direction $\varphi_F = 0^\circ$. It shows that the direction of the force stays constant and almost no torque is generated with the bearing current. The dashed line shows the force obtained by 2-D simulation.

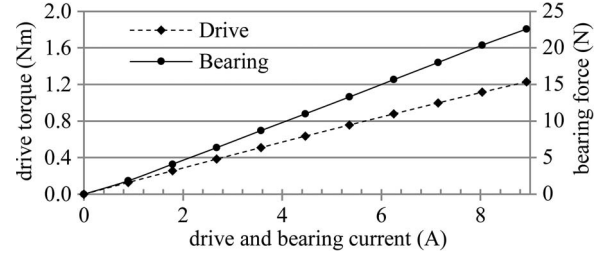


Fig. 11. Force and torque simulated for different bearing and drive currents at the rotor angle $\theta = 0^\circ$. The simulation shows a linear dependency of drive and bearing currents with the resulting force and torque. The results are independent of the rotor angle.

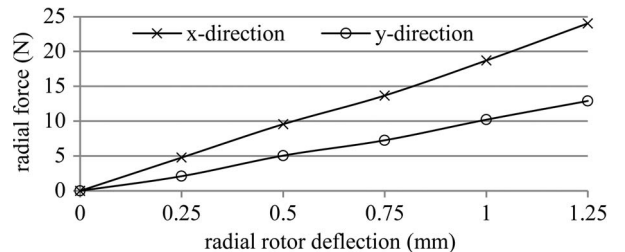


Fig. 12. Simulated reaction forces on the rotor due to deflection in the radial directions x and y with a rotor angle of $\theta = 0^\circ$. As the forces are positive, the bearing is instable in radial direction.

The simulations also confirmed the anisotropy of the passive bearing stiffnesses. The forces acting on the rotor as a result of radial deflection and tilting are shown in Figs. 12 and 13. The destabilizing radial bearing stiffness is about two times higher in magnetization direction than perpendicular to the magnetization. The same effect occurs with the tilting stiffness. This

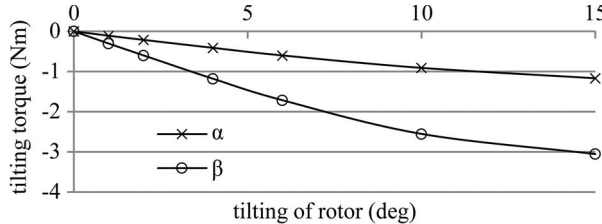


Fig. 13. Simulated reaction torque on the rotor due to tilting around magnetization axis (α) and perpendicular to it (β).

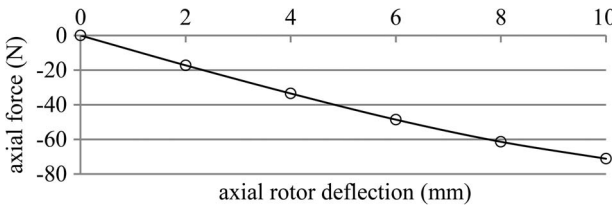


Fig. 14. Simulated reaction force on the rotor due to axial deflection of the rotor.



Fig. 15. Test setup with stator, levitated rotor, and sensor board. Driven by the six coils wound on the white stator ring, the metallic annular rotor in the middle can be levitated and spun. The green sensor board pre-processes signals from hall- and eddy-current sensors.

will lead to two different tilting resonance frequencies, as will be verified in the experiment (see Section VI). Nevertheless, the passive bearing stiffnesses act over a wide deflection range in axial (Fig. 14) and tilting direction and generate sufficient torque and bearing forces for a stable operation.

VI. PRACTICAL RESULTS

A. Prototype

To demonstrate the feasibility of the proposed concept, a prototype of the drive was built (see Fig. 15 and Table IV). It consists of a ring-shaped core that is embedded in plastic trays for the windings. Every three coils, with 112 windings each, are connected in one star point. The annular rotor in the center holds the magnets between two stainless steel shells.

The bearingless motor is controlled by an inverter, which mainly consists of a digital signal processor realizing the control algorithms, and two IGBT modules. Each IGBT module contains six power switches and powers a star system of three coils. The modules are fed by a dc link voltage of around 325 V.



Fig. 16. Spinning rotor seen from above. To each side, the rotor has a free air gap of 1 mm. Rotational speeds of up to 20 000 r/min are tested.

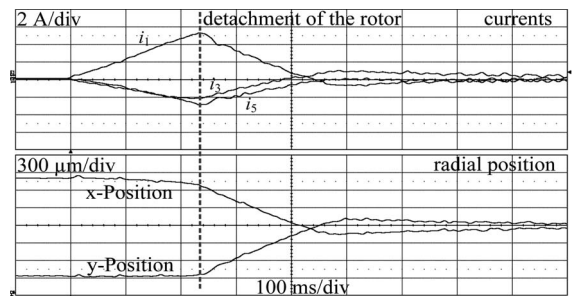


Fig. 17. Coil currents and rotor position measured during start of levitation. The current rises until the rotor starts to move towards its middle position.

When the rotor is levitated, there is a free air gap of 1 mm at each side and more than 5 mm to the bottom, so that a contact-free operation is guaranteed. Fig. 16 shows the spinning rotor seen from above surrounded by the six coils. With this configuration, a rotational speed of 20 000 r/min was reached smoothly, which is the speed limit given by the mechanical strength of the rotor.

B. Performance

When the device is turned off, the rotor is attached to the stator, attracted by the passive magnetic forces. Before starting to spin the rotor, it has to be actively positioned to the center. This startup process is shown in Fig. 17, where the currents in three of the six coils during the startup process along with the radial rotor position are depicted. The currents of the other three coils are the same as the shown currents, as only bearing forces are generated during startup. In the shown “soft start” mode, the control algorithm increases the current until the rotor starts to move toward the center position. In this position, the magnetic forces on the rotor are approximately zero, so that the bearing currents decrease. The measured current needed for the start of the levitation is about

$$\hat{I}_{B,\text{start}} = 5.3 \text{ A}$$

which is nearly 30% smaller than the simulated value of 7.4 A (Table V). The reason for this deviation is that the passive radial stiffness is also about 30% lower than simulated, as can be seen later.

The force coefficient of the prototype was measured in a static experiment. The motor was operated in upright position (i.e., horizontal z -axis) with levitated but not rotating rotor, so

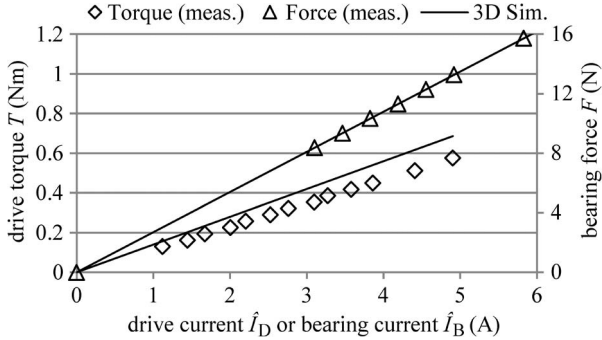


Fig. 18. Measured drive or bearing current at the prototype, while static torques or forces are applied to the rotor, respectively. The values are compared to the 3-D simulation results. The measured forces fit exactly to the simulated value, while the torque is around 17% lower.

that the gravity applies a force on the rotor in y -direction. The resulting bearing current

$$\hat{I}_{B,\text{meas}} = \frac{1}{2}(i_1 + i_4) \text{ at } \theta = 0^\circ, \varphi_F = 90^\circ$$

is measured by the mean value of the coil currents i_1 and i_4 at the rotor position of $\theta = 0^\circ$. With additional weights, higher forces are applied to the rotor. The resulting bearing currents for the different applied forces are shown in Fig. 18. It shows, that the measurements fit nearly exactly to the simulated force coefficient.

In a similar way, the drive coefficient is determined. In the same motor position, a lever is mounted to the levitated rotor. With different weights, different torques are applied to the rotor. The drive current can be measured by

$$\hat{I}_{D,\text{meas}} = \frac{1}{2}(i_1 - i_4) \text{ at } \theta = 0^\circ.$$

The results show linear dependency of torque and drive current with a drive coefficient of about $k_{T,\text{meas}} = 0.116 \text{ Nm/A}$, which is about 17% lower than simulated (see Fig. 18).

Additionally, the passive radial stiffnesses are measured by displacing the rotor from its middle position with an offset controlled by the electronics in d- and q-direction. The measured bearing currents are converted into bearing forces by the before measured force coefficient. The results are shown in Fig. 19. It shows that the radial stiffnesses are about 30% lower than in the simulation. We assume that this is due to different material characteristics of magnet and stator core material, compared to the values assumed in the simulation. Previous investigations have shown that flat motor topologies with big air gaps tend to be prone to deviations in material properties in regard to the passive stiffnesses. The later on measured tilting and axial stiffnesses show the same deviation. All measurement results are summarized and compared to the 3-D simulation results in Table VI.

The acceleration and deceleration process of the motor is shown in Fig. 20. The first small peak in coil and bearing current marks the startup of the levitation. After that, the currents with increasing frequency are the drive currents generating the torque. In this case, the controller limits the acceleration to a ramp step limit of 2000 (r/min)/s. This might be reasonable

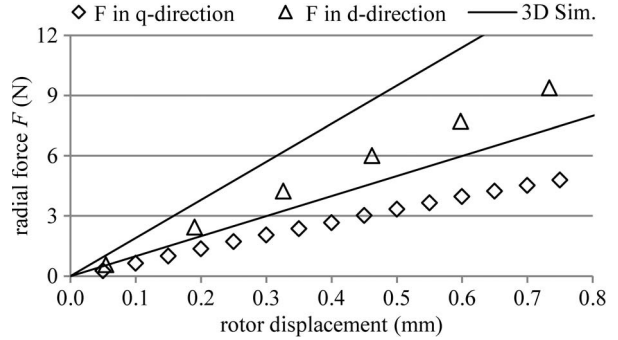


Fig. 19. Measured bearing forces, while the rotor is displaced in magnetization direction (d-direction) or perpendicular (q-direction). The measurements are compared to the 3-D simulation results. It shows that both radial stiffnesses are around 30% lower than simulated.

TABLE VI
COMPARISON OF MEASUREMENTS WITH SIMULATION RESULTS

	Measurement	3D Sim.
force coefficient	k_F	2.71 N/A
torque coefficient	k_T	0.117 Nm/A
startup current	$\hat{I}_{B,\text{start}}$	5.3 A
axial resonance	f_z	12.7 Hz
tilting resonance	f_α	12.4 Hz
	f_β	22.5 Hz
tilting stiffness	c_α	0.073 Nm/deg
	c_β	0.239 Nm/deg
axial stiffness	c_z	5.44 N/mm
	c_d	-12.5 N/mm
radial stiffness	c_q	-7.1 N/mm

for some applications to avoid high acceleration forces and high input power. During constant speed, the drive current is nearly zero, as there is hardly any drive torque. Only very little power is needed to compensate the motor and air friction losses, which are very small. At the deceleration phase the controller generates maximal torque, but the drive currents are limited exemplarily to an amplitude of $\hat{I}_D = 5 \text{ A}$. This is useful e.g., at an emergency shutdown, where the deceleration shall be as fast as possible, but currents have to be limited to have enough capability left for a safe bearing operation and to protect the power electronics.

The position signal in Fig. 20, measured by the eddy current sensors of the setup, shows two resonance frequencies at lower speeds. As the eddy current sensors are prone to tilting displacements of the rotor, this resonance can be ascribed to the tilting resonances of the rotor. During acceleration and deceleration, the measured deflection of the rotor is in the range of $\pm 0.4 \text{ mm}$. Beyond the resonance frequencies, the deflection amplitude is nearly constant and very small ($\pm 70 \mu\text{m}$). This is due to the control algorithm, which does not spin the rotor around its geometrical center but tries to minimize the bearing currents by rotating around the center of mass in order to minimize power losses. As the rotor is not manufactured perfectly, the geometrical center and the center of mass are not identical. Therefore, the rotor position shows a constant deflection amplitude.

In another experiment, the tilting and axial displacements are measured during acceleration (see Fig. 21). This was done by two laser sensors, measuring the displacement at two opposite points at the rotor. The tilting signal is calculated by the difference of the signals and the distance between the sensors. The

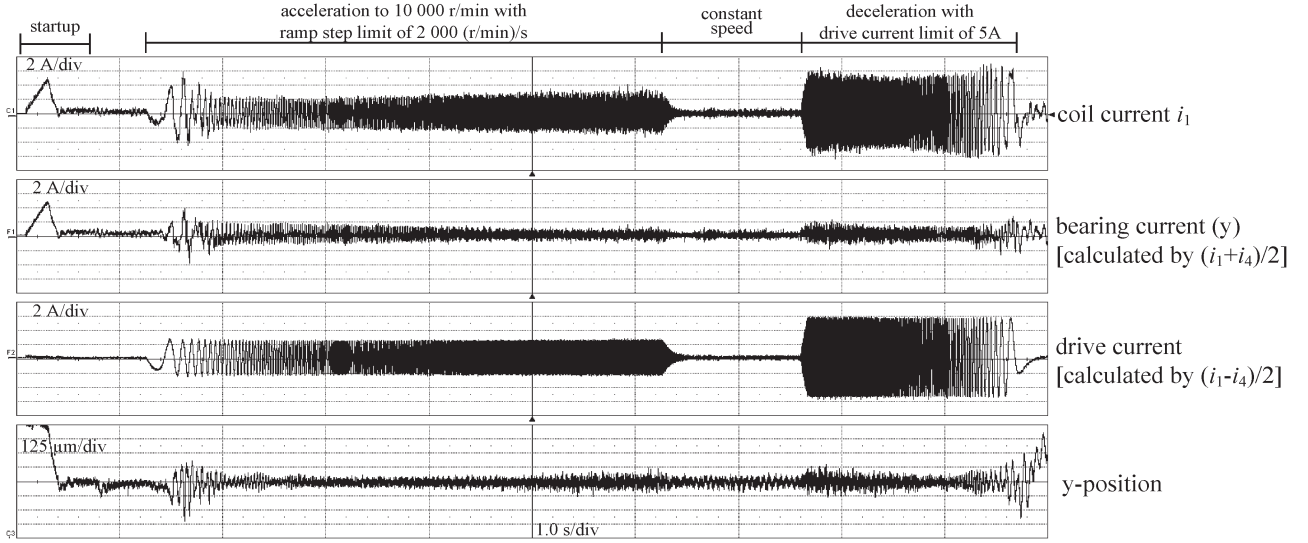


Fig. 20. Bearing current, drive current, and radial position during startup, acceleration to 10 000 r/min, and deceleration.

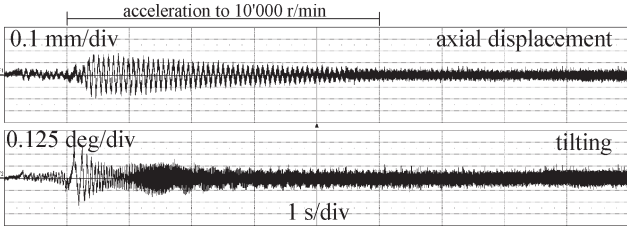


Fig. 21. Axial displacement and tilting of the rotor during acceleration to 10 000 r/min and constant speed.

mean value of both sensor signals gives the axial displacement. Here, again, two tilting resonances can be seen at the beginning of the acceleration. Additionally, the axial resonance is induced at low speeds and subsides quite slowly. After passing the resonances, the axial displacement is around $\pm 50 \mu\text{m}$ and the tilting around $\pm 0.12^\circ$.

To test the drive performance and to ensure that the drive controller is correctly adjusted, the acceleration time from standstill to 10 000 r/min ($\Delta\omega = 1047 \text{ s}^{-1}$) was measured ($\Delta t_{\text{acc},0-10000} = 5.0 \text{ s}$). With the moment of inertia $J = 1.33 \text{ gm}^2$ of the rotor, the mean torque acting on the rotor during acceleration results in

$$T_{\text{acc}} = J\dot{\omega} = J\frac{\Delta\omega}{\Delta t_{\text{acc},0-10000}} = 0.278 \text{ Nm.}$$

With a measured mean current amplitude during acceleration of $\hat{I}_{D,\text{acc}} = 2.33 \text{ A}$, the torque coefficient results in

$$k_{T,\text{acc}} = \frac{T_{\text{acc}}}{\hat{I}_{D,\text{acc}}} = 0.120 \text{ Nm/A.}$$

The acceleration torque is even slightly higher than measured in the static experiment before, which might be due to measurement inaccuracies. With this, the drive performance is proven in standstill and during acceleration.

The highest rotational speed tested is 20 000 r/min, as this is the rated speed for the motor design. To verify the speed, the signal of the hall sensor, which has the same frequency as the

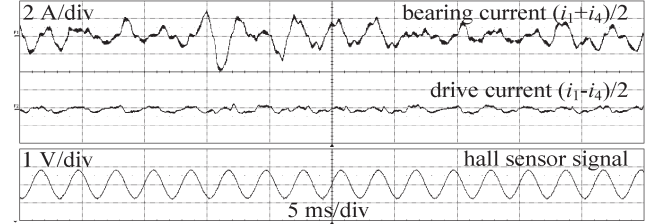


Fig. 22. Rotation at 20 000 r/min: Bearing and drive current are calculated from coil currents i_1 and i_4 . The hall sensor signal indicates the rotational speed.

mechanical rotation, as well as bearing and drive current were measured (see Fig. 22). Additionally, the rotational speed was checked with a stroboscope.

C. Power Consumption and Losses

To evaluate the losses of the bearingless motor, the overall power consumption of the system, including electronics and motor, was measured at the power input of the inverter with a wattmeter at no-load operation. The power consumption of the motor, including motor and bearing losses, was measured at the coils with an oscilloscope. Thus, the power consumption of the inverter and of the motor could be separated. The results are shown in Fig. 23. All power measurements are conducted in a no-load situation. At the top speed of 20 000 r/min, the overall power input to the system, including inverter and bearingless motor, is 111 W. The power input to the coils is 76 W, which are the motor and bearing losses.

The losses of the inverter are composed of a constant part of around 22 W and a load-dependent part, which is rising by about 17 W per 100 W electrical output power.

The losses of the motor are highly dependent on the rotational speed. They consist of iron losses in the stator and in the rotor as well as air friction losses. It appeared that the copper losses are neglectable in the no-load case, as the currents in the coils are around 0.7 A rms at top speed. With a resistance of 0.35Ω per coil, the copper losses of the motor are around 1 W.

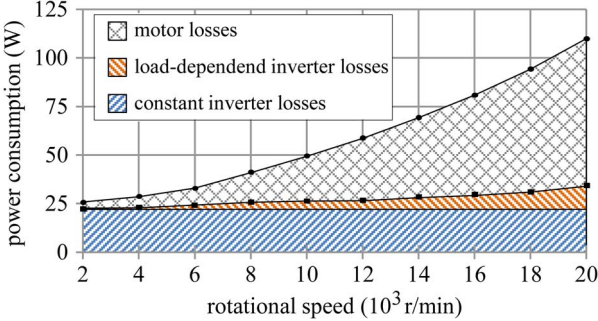


Fig. 23. Measured energy consumption of the motor and the inverter up to 20 000 r/min in no-load situation. The motor losses consist of iron losses in the stator and in the rotor as well as air friction losses. The maximal copper losses in the no-load case are around 1 W and are not shown in the diagram.

To predict the efficiency in the load case of the motor, we assume a mechanical load of 1 kW at 20 000 r/min. Then, the controller losses will increase by 170 W. The motor currents will rise to 3.1 A rms in each coil, the approximate copper losses will be 20 W. The iron and air friction losses are supposed to be independent of the load, because the magnetic field does not rise significantly with higher motor currents, which was tested in simulation. Adding these additional losses to the 111 W at no load operation, the predicted total losses are 301 W at a mechanical output power of 1 kW. Of these losses, 96 W occurs in the motor and 205 W in the inverter. This results in an efficiency of 77%. The controller has a rated power output of 2 kW, so the motor power could be increased even more.

D. Stability

At low rotational speeds of around 500–2000 r/min, the rotor shows two resonance frequency areas. The rigid body resonance frequencies have been measured in standstill by laser sensors and manual stimulation (see Table VI). The first tilting resonance and the axial resonance are nearly at the same frequency. With the second tilting resonance frequency, the two resonances during acceleration can be explained. With the calculated moment of inertia in the two tilting axes as well with the mass, the stiffness values of the passive bearing are calculated by

$$c_z = (2\pi f_z)^2 \cdot m$$

$$c_{\alpha,\beta} = (2\pi f_{\alpha,\beta})^2 \cdot J_{\alpha,\beta}.$$

The values are 20%–36% lower than in the simulation, which is similar to the deviation of the radial stiffnesses. We assume that this is due to deviations of the material properties of magnet and stator core material, compared to the values assumed in the simulation.

With higher speeds, no resonances and instabilities are observed, and the prototype shows a stable and smooth operation behavior and a low noise level. Therefore, probably even lower stiffness would be possible, which allows smaller magnets and thus a more lightweight and robust rotor and consequently even higher rotational speeds. However, smaller magnets would also reduce the achievable bearing forces and drive torque, but due to the lower flux density the iron losses would be reduced, too.

VII. CONCLUSION

Summarizing, the working principle as well as the current commands for bearing and motor operation is shown, and the theoretical considerations are proven by simulation results. The proposed analytical calculations of bearing and drive inductance allow for easy assessment of the dynamic properties of the bearingless motor, which is confirmed by measurements.

The measured force coefficient fits exactly to the simulation; the torque coefficient is only slightly lower. Higher deviations between simulation and measurements of about 30% are observed at the passive stiffnesses. We assume that this is due to the not exactly known material properties of the prototype. However, the measurements confirmed linear behavior of drive torque, bearing force, and radial stiffness, which might be the reason for the good operational behavior and the easy controllability of the prototype. Finally, the designed prototype successfully operates at the designed rotational speed of 20 000 rpm. Altogether, the feasibility of this slotless bearingless drive concept for the application in high-speed and high-purity applications is proved. Considering the large air gap and the slotless design, the motor generates sufficiently high torque to be eligible for the mentioned applications and shows a satisfying stability behavior.

REFERENCES

- [1] X. Sun, L. Chen, and Z. Yang, "Overview of bearingless permanent-magnet synchronous motors," *IEEE Trans. Ind. Electron.*, vol. 60, no. 12, pp. 5528–5538, Dec. 2013.
- [2] J. Asama, Y. Hamasaki, T. Oiwa, and A. Chiba, "Proposal and analysis of a novel single-drive bearingless motor," *IEEE Trans. Ind. Electron.*, vol. 60, no. 1, pp. 129–138, Jan. 2013.
- [3] S.-M. Yang and M.-S. Huang, "Design and implementation of a magnetically levitated single-axis controlled axial blood pump," *IEEE Trans. Ind. Electron.*, vol. 56, no. 6, pp. 2213–2219, Jun. 2009.
- [4] S. Silber *et al.*, "High-speed drive for textile rotor spinning applications," *IEEE Trans. Ind. Electron.*, vol. 61, no. 6, pp. 2990–2997, Jun. 2014.
- [5] T. Reichert, T. Nussbaumer, and J. W. Kolar, "Bearingless 300-W PMSM for bioreactor mixing," *IEEE Trans. Ind. Electron.*, vol. 59, no. 3, pp. 1376–1388, Mar. 2012.
- [6] B. Warberger, R. Kaelin, T. Nussbaumer, and J. W. Kolar, "50-Nm/2500-W bearingless motor for high-purity pharmaceutical mixing," *IEEE Trans. Ind. Electron.*, vol. 59, no. 5, pp. 2236–2247, May 2012.
- [7] M. Ooshima, S. Kitazawa, A. Chiba, T. Fukao, and D. G. Dorrell, "Design and analyses of a coreless-stator-type bearingless motor/generator for clean energy generation and storage systems," *IEEE Trans. Magn.*, vol. 42, no. 10, pp. 3461–3463, Oct. 2006.
- [8] P. Karutz, T. Nussbaumer, W. Gruber, and J. W. Kolar, "Novel magnetically levitated two-level motor," *IEEE/ASME Trans. Mechatronics*, vol. 13, no. 6, pp. 658–668, Dec. 2008.
- [9] R. Schoeb and N. Barletta, "Principle and application of a bearingless slice motor," *JSME Int. J. Ser. C, Mech. Syst. Mach. Elements Manuf.*, vol. 40, no. 4, pp. 593–598, Dec. 1997.
- [10] L. Chen and W. Hofmann, "Speed regulation technique of one bearingless 8/6 switched reluctance motor with simpler single winding structure," *IEEE Trans. Ind. Electron.*, vol. 59, no. 6, pp. 2592–2600, Jun. 2012.
- [11] F. Zürcher, T. Nussbaumer, and J. W. Kolar, "Motor torque and magnetic levitation force generation in bearingless brushless multipole motors," *IEEE/ASME Trans. Mechatronics*, vol. 17, no. 6, pp. 1088–1097, Dec. 2012.
- [12] C. M. Zingerli, J. W. Kolar, and T. Nussbaumer, "Analysis of rotor shell losses in a magnetically levitated homopolar hollow-shaft permanent magnet synchronous motor," in *Proc. 7th IPMC*, 2012, pp. 286–291.
- [13] Z. Ren, L. S. Stephens, and A. V. Radun, "Improvements on winding flux models for a slotless self-bearing motor," *IEEE Trans. Magn.*, vol. 42, no. 7, pp. 1838–1848, Jul. 2006.
- [14] T. Baumgartner, R. M. Burkart, and J. W. Kolar, "Analysis and design of a 300-W 500 000-r/min slotless self-bearing permanent-magnet motor," *IEEE Trans. Ind. Electron.*, vol. 61, no. 8, pp. 4326–4336, Aug. 2014.

- [15] H. Mitterhofer, W. Gruber, and W. Amrhein, "On the high speed capacity of bearingless drives," *IEEE Trans. Ind. Electron.*, vol. 61, no. 6, pp. 3119–3126, Jun. 2014.
- [16] H. Mitterhofer and W. Amrhein, "Design aspects and test results of a high speed bearingless drive," in *Proc. 9th IEEE Int. Conf. PEDS*, 2011, pp. 705–710.
- [17] H. Mitterhofer and W. Amrhein, "Motion control strategy and operational behaviour of a high speed bearingless disc drive," in *Proc. IET Power Electron., Mach. Drives Conf.*, 2012, pp. 1–6.
- [18] H. Sugimoto *et al.*, "Radial force characteristics of multi-consequent-pole bearingless motor," in *Proc. ICEMS*, 2008, pp. 3644–3649.
- [19] J. Asama, R. Nakamura, H. Sugimoto, and A. Chiba, "Evaluation of magnetic suspension performance in a multi-consequent-pole bearingless motor," *IEEE Trans. Magn.*, vol. 47, no. 10, pp. 4262–4265, Oct. 2011.
- [20] H. Lee, S. Yoo, and M. D. Noh, "Toroidally-wound self-bearing BLDC motor with Lorentz force," *IEEE Trans. Magn.*, vol. 46, no. 6, pp. 2148–2151, Jun. 2010.
- [21] T. Nussbaumer, P. Karutz, F. Zurcher, and J. W. Kolar, "Magnetically levitated slice motors—An overview," *IEEE Trans. Ind. Appl.*, vol. 47, no. 2, pp. 754–766, Mar./Apr. 2011.
- [22] J. Luomi, C. Zwysig, A. Looser, and J. W. Kolar, "Efficiency optimization of a 100-W 500 000-r/min permanent-magnet machine including air-friction losses," *IEEE Trans. Ind. Appl.*, vol. 45, no. 4, pp. 1368–1377, Jul./Aug. 2009.



Daniel Steinert (S'13) received the M.Sc. degree in mechatronics from the Dresden University of Technology, Dresden, Germany, in 2012, where he focused on micro-mechatronics and precision engineering. In his master's thesis, he analyzed the electro-mechano-acoustic transducer properties of piezoelectric bending plates. Since 2012, he has been with the Power Electronic Systems Laboratory, Swiss Federal Institute of Technology (ETH) Zurich, Zurich, Switzerland, as a Ph.D. student, where he works on high-speed bearingless motors.

His current research is focused on bearingless motor topologies, control concepts, losses, and applications of bearingless motors.



Thomas Nussbaumer (S'02–M'06) was born in Vienna, Austria, in 1975. He received the M.Sc. degree (Hons.) in electrical engineering from the University of Technology Vienna, Vienna, Austria, in 2001, and the Ph.D. degree from the Power Electronic Systems (PES) Laboratory, Swiss Federal Institute of Technology (ETH) Zurich, Zurich, Switzerland, in 2004.

From 2001 to 2006, he was with the PES, where he was involved in research on modeling, design, and control of three-phase rectifiers, power factor correction techniques, and electromagnetic compatibility. Since 2006, he has been with Levitronix GmbH, Zurich, where he is currently involved in research on bearingless motors, magnetic levitation, and permanent-magnet motor drives for the semiconductor and biotechnology industries. His current research is focused on compact and high-performance mechatronic systems, including novel power electronics topologies, control techniques, drive systems, sensor technologies, electromagnetic interference, and thermal aspects.



Johann W. Kolar (M'89–SM'04–F'10) received the M.Sc. and Ph.D. degrees (*summa cum laude*) from the University of Technology Vienna, Vienna, Austria, in 1997 and 1998, respectively.

Since 1982, he has been working as an international consultant in the fields of power electronics, industrial electronics, and high-performance drives. Currently, he is a Full Professor and the Head of the Power Electronic Systems Laboratory at the Swiss Federal Institute of Technology (ETH) Zurich, Zurich, Switzerland. He has proposed numerous novel PWM converter topologies and modulation and control concepts, e.g., the Vienna Rectifier, the Swiss Rectifier, and the AC–AC Sparse Matrix Converter. He has published over 550 scientific papers in international journals and conference proceedings and has filed more than 110 patents. The focus of his current research is on AC–AC and AC–DC converter topologies with low effects on the mains, on the realization of ultra-compact/efficient converter modules employing latest power semiconductor technology (SiC and GaN), Power Supplies on Chip, multi-domain/scale modeling/simulation and multi-objective optimization, and ultra-high speed and bearingless motors.

Prof. Kolar received nine IEEE Transactions Prize Paper Awards and eight IEEE Conference Prize Paper Awards.